JOURNAL OF GEOPHYSICAL RESEARCH, VOL. 98, NO. A1, PAGES 293–310, JANUARY 1, 1993

Observations of Nightside Auroral Cavities

RICHARD A. DOE[1], MICHAEL MENDILLO[1], JAMES F. VICKREY[2], LAWRENCE J. ZANETTI[3] AND RICHARD W. EASTES[4]

Radar observations of field-aligned auroral F region density depletions (cavities) have been identified in a portion of the Sondre Stromfjord incoherent scatter radar (ISR) data base covering the period February 1986 to January 1988. These "auroral cavities" are nightside phenomena with localized, field-aligned F region density depletions of 20 to 70 percent below surrounding values. They occur during moderate to quiet geomagnetic conditions when the poleward edge of the auroral oval is within view of Sondre Stromfjord. Seasonally, they are a wintertime phenomena occurring just poleward of the statistical auroral oval. Unlike the previously reported "polar hole," the average width of the cavities is less than 100 km. Case studies show that the cavities closely track the poleward edge of the most poleward auroral arc. Sequential radar scans show that cavities appear on time scales as short as several minutes, suggestive of local electrodynamic formation or rapid transport. Data from January 24, 1987, collected during coordinated optical, radar, and satellite observations spanning an hour of local time, were examined for possible cavity formation mechanisms. The cavity formation processes examined herein include locally enhanced chemical loss, vertical diffusion, drifting horizontal gradients in the background plasma, and evacuation as a result of field-aligned currents. The formation time scales, calculated evacuation fluxes, close proximity to E region aurora, and field-aligned current signatures seen in magnetometer and radar observations suggest a strong association of the cavities with upward flowing electrons carrying region 1 downward field-aligned currents.

1. INTRODUCTION

The Sondre Stromfjord incoherent scatter radar has measured electron density structure associated with plasma dynamics by typically searching for enhancements rather than voids [*Vickrey et al.*, 1980; *Tsunoda*, 1988, and references therein]. Within a uniform plasma background, however, the radar can also effectively track the motion and evolution of density depletions within its field of view. This study presents observations between February 1986 and January 1988, of medium-scale field-aligned F region plasma density depletions in radar scans along the magnetic meridian. These observations often indicate a region of depleted plasma density that is confined in latitude, but extended in altitude (along the magnetic field). Most often the depletion is located near the poleward edge of the most poleward E layer arc.

An example of a nightside auroral cavity is presented in Plate 1 for the geomagnetically quiet ($K_p = 1$) evening of January 27, 1987. The four meridional electron density panels span 20 min centered around 0120 magnetic local time (MLT) at 0320 UT. Each panel is a vertical slice through the geomagnetic meridian with 1000 km of north/south distance along the horizontal axis and 600 km of altitude along the vertical axis. The log of electron density in this plane is color coded from 4.6 to 6.0 electrons cm^{-3}. Auroral E region ionization is clearly seen to the south and a polar cap F region with an $N_e \sim 6.0 \times 10^4$ electrons cm^{-3} is visible to the north. Between these two regions is a field-aligned depletion 40 percent below the density of the adjacent polar cap F region. This feature is an example of an auroral cavity. The local geomagnetic field lines spanning the cavity have been superimposed on the fourth panel for clarity.

All measurements in this study are made near the poleward edge of the auroral oval, and thus the potential exists for confusion with the classic high-latitude trough, or "polar hole." In order to avoid this confusion and set the context for the discussion of "auroral cavities," a brief review of past polar hole observations is appropriate. Large-scale plasma density depletions observed at high latitudes in the polar cap (70° to 80° magnetic) were first described as the "polar hole" by *Brinton et al.* [1978] on the basis of thermal plasma density measurements made by the AE-C satellite at 300 km altitude. Subsequent higher-altitude measurements of auroral kilometric radiation associated with these depleted electron densities by *Benson and Calvert* [1979] and *Persoon et al.* [1988] have established the polar hole as a regular feature of the Earth's nightside polar cap. Others have postulated similar depletions on Uranus and Neptune [*Farrel et al.*, 1991]. Modeling studies by *Sojka et al.* [1981] have been successful in reproducing the wintertime observations of this depletion by allowing chemical decay to work upon polar plasma tied to slowly convecting flux tubes that are only weakly illuminated (by resonantly scattered UV). Outstanding characteristics of this polar hole include its large latitudinal width, 6° to 10°, and low F region density with N_e typically 3×10^2 to 1×10^3 electrons cm^{-3} (at F region peak). In contrast, the radar observations of nightside auroral cavities are relatively narrow, typically less than 1°, with average densities of $\sim 1 \times 10^4$ electrons cm^{-3}. These densities represent 20 to 70 percent depletions below those measured simultaneously in the adjacent polar cap and are quite moderate when compared to the ratio of polar hole to polar cap densities previously reported. The salient features of the auroral cavities are their field-aligned shape,

[1]Center for Space Physics, Boston University, Boston, Massachusetts
[2]Geoscience and Engineering Center, SRI International, Menlo Park, California
[3]Applied Physics Laboratory, Johns Hopkins University, Laurel, Maryland
[4]Geophysics Directorate, Phillips Laboratory, Hanscom Air Force Base, Massachusetts

Paper number 92JA02004.
0148-0227/93/92JA-02004$05.00

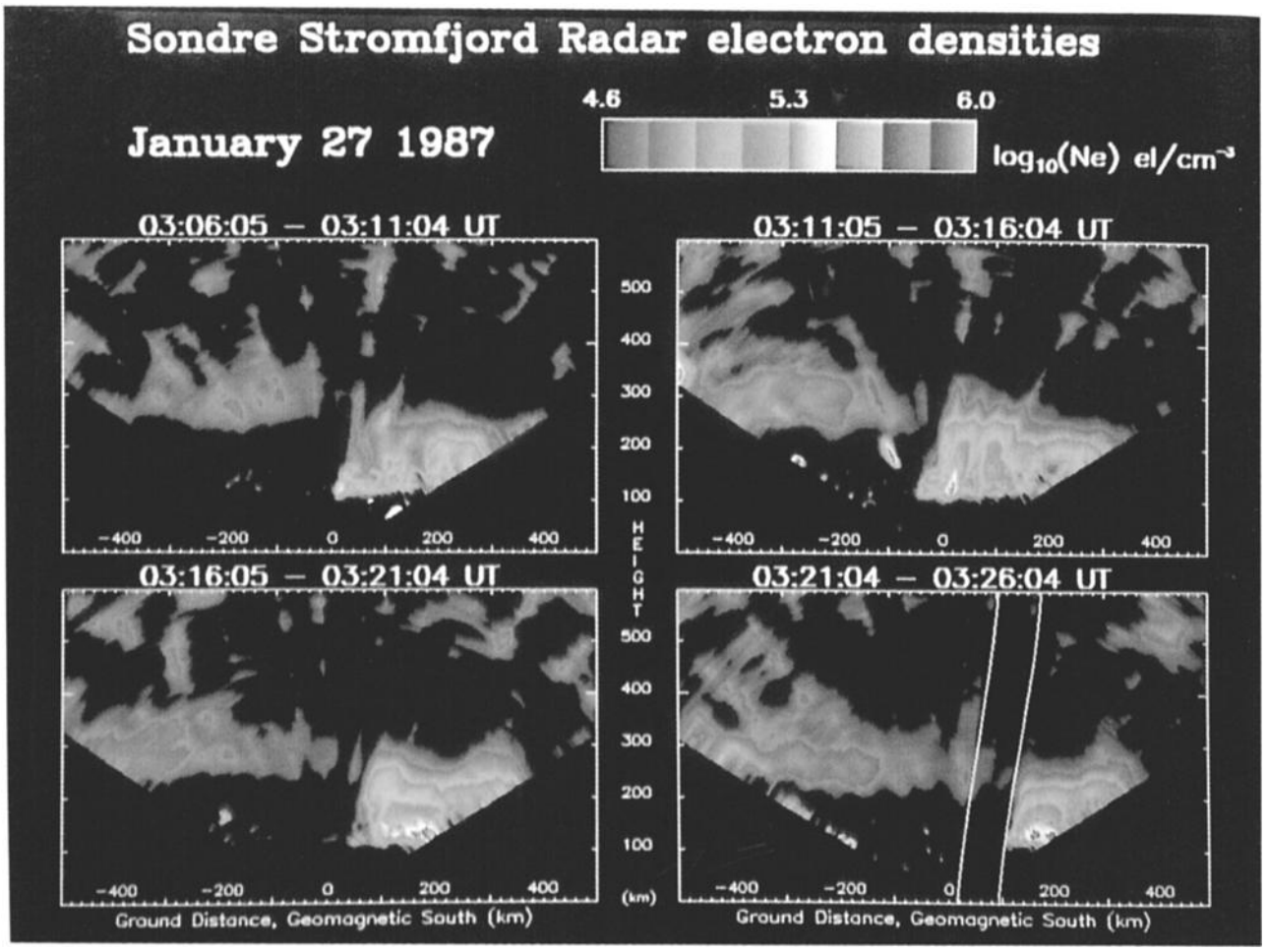

Plate. 1. A nightside auroral cavity seen in four sequential meridional radar scans on January 27, 1987. Each scan spans 1000 km along the horizontal axis and 600 km along the vertical axis. The log of electron density from 4.6 to 6.0 electrons cm^{-3} has been color-coded as indicated. This cavity is wedged between dense auroral E region plasma south of the radar and a less dense polar cap F region to the north. Magnetic field lines from the PACE model [*Baker and Wing*, 1989] have been superimposed on the cavity in the fourth scan to emphasize the field-aligned nature of the depletion.

close proximity to E region density enhancements and relatively short ($\sim$ 300 s) formation times.

Some observations of electron density depletions at the poleward edge of the auroral oval, of magnitude comparable to those reported in this study, have been reported previously. *Basu et al.* [1984] discuss density depressions of this scale and magnitude from an overflight of the AE-D satellite in 1975. They measured depleted electron densities well correlated with an ion temperature enhancement and proposed that enhanced chemical loss was the formation mechanism. *Robinson and Mende* [1990] also invoke chemical loss in their study of F region density structure that spans a dusk sector E region arc. They show that a south to north F region density gradient will result from recombination acting on plasma that transits a convection reversal at radar zenith. Unlike auroral cavities, however, their density gradient was not spatially confined to the poleward edge of the E region arc, and was much wider ($\sim$ 6°) than the typical cavity ($\sim$ 1°). *Winser et al.* [1986] reported observations of depletion structure of the same magnitude as those found in auroral cavities, and attributed them to local ion heating at magnetic midnight. These depletions were equatorward of, and again much wider than, the narrow auroral cavities reported herein. *Weber et al.* [1991] describe an F region density depletion observed directly above an evening sector E region arc. This depletion was observed in the absence of an ion temperature enhancement, collocated with a convection shear and in a region of zero vertical ion outflow. The close association of their F region depletion with the E region arc, while describing a different scenario than that observed for auroral cavities, may be a related phenomena.

Rodger et al. [1991], in their review of ionospheric troughs, raised the question of whether density depressions are the result of plasma evacuation, transport or decay, or are simply a normal polar cap ionosphere "caught between" density enhancements. If cavities result from physical processes that decrease density, rather than being gaps between enhancements, then the background polar cap F region densities (within which cavities are observed) should be well below those reported for ionization enhancements. The background polar cap density of 7.8×10^4 electrons cm^{-3}, addressed in section 2, is a factor of 2 below the typical sun-aligned arc densities reported by *Carlson et al.* [1984], a factor of 3 below the auroral blob density reported by *Tsunoda* [1988], and a factor of 10 below the F region patch density reported by *Buchau et al.* [1983]. This suggests a depletive mechanism for cavity formation.

The following sections present a statistical overview of cavity observations over a 2-year period and a detailed, multidiagnostic case study, respectively. The measurements

made during the January 24, 1987, case study will be used to assess the relative efficiency of four cavity formation mechanisms.

2. OBSERVATIONS: AVERAGE MORPHOLOGY AND OCCURRENCE PATTERN

2.1. *Description of Data Base*

The data base of Sondre Stromfjord radar elevation scans made in conjunction with overflights of the HILAT and Polar BEAR satellites is well suited for the study of auroral cavities. For an average of four campaigns each month, the radar performed a set of elevation scans in the magnetic meridional and east-west planes. Each campaign ran for approximately 4 hours centered on the satellite overpass. The 5-min meridional scans were made approximately 50 percent of the time during each campaign. For maximum time resolution the radar often executed alternating south-to-north and north-to-south scans in a "windshield wiper" motion. This high time resolution was particularly useful for observations of cavity formation and their subsequent evolution. The five minute scans over 120° of elevation were integrated in 10 s intervals to give 4° angular resolution. At 300 km altitude the resultant arc length of 20 km is comparable to the ~ 50-km range resolution and gives reasonably "square" sample resolution at F region altitudes. This large data base also makes possible the comparison of radar data with occasionally coincident satellite UV imager, total electron content (TEC) and magnetometer measurements. Such a comparison will be exploited in the case study of section 3.

2.2. *Selection Criteria*

A search was made for auroral cavities within the approximately 1500 individual radar scans that make up the HILAT/Polar BEAR radar data base. Meridional scans which contained F region ionization alone, as well as daytime scans showed no evidence for auroral cavities. Nightside scans which contained auroral E region ionization were then selected for close inspection. Scans with field-aligned cavities were selected by eye with the criteria that the depletions should be at least 20 percent below the surrounding polar cap F region density. Quite often the cavities were in close proximity to a structured polar cap F region, making the determination of relative percent depletion difficult. Therefore scans with significant density structure such as drifting blobs, patches and polar cap arcs were excluded in order to insure a relatively unstructured polar cap F region. Because of the ubiquity of such structure, this criteria eliminated many scans. However, for 29 of the remaining radar scans, cavities were either visible during the first elevation scan or formed during the course of the experiment.

2.3. *Statistical Results*

Figure 1 shows the monthly distribution of auroral cavity observations as a histogram of 92 coordinated radar-HILAT/Polar BEAR campaigns during the study period. January was the only month sampled for three (rather than two) consecutive years and shows both a peak in the number of experiments run and in cavity observations. Figures 2a and 2b show cavity occurrence on grids of polar MLT versus invariant latitude for each individual radar scan in which a cavity was observed. The data points are identical in both

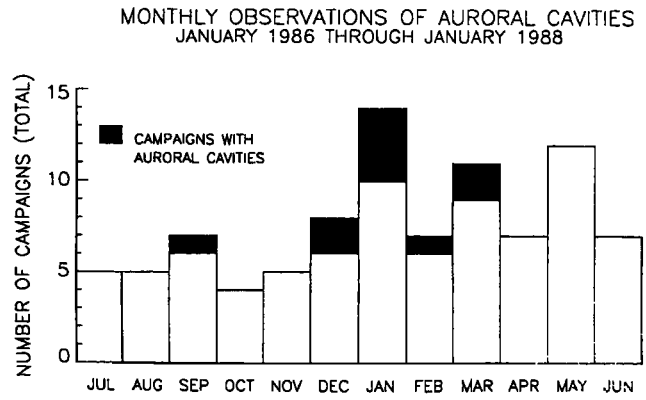

Fig. 1. Histogram of 92 coordinated HILAT/Polar BEAR radar experiments. Cavity observations are indicated by dark shading.

grids. The quiet time oval of *Feldstein and Starkov* [1967] is shown in Figure 2a and the region 1 and 2 nightime current systems of *Iijima and Potemra [1976]* are shown in Figure 2b. These overlays emphasize that observations of auroral cavities are at the equatorward boundary of the statistical nightside polar cap. The requirement that both auroral E region and polar cap F region ionization be present at latitudes visible from Sondre Stromfjord is a de facto selection of low to moderate geomagnetic activity.

Table 1 completes this statistical survey by describing the background conditions and specific cavity character for each individual radar scan. Columns one through four catalog the date, K_p index, interplanetary magnetic field (IMF) and MLT associated with each observation. Columns five and six list the mean polar cap electron density outside the cavity and percent depletion in the cavity, relative to this mean. Column seven shows the width in kilometers. For the several cases where cavities remain within the radar field of view

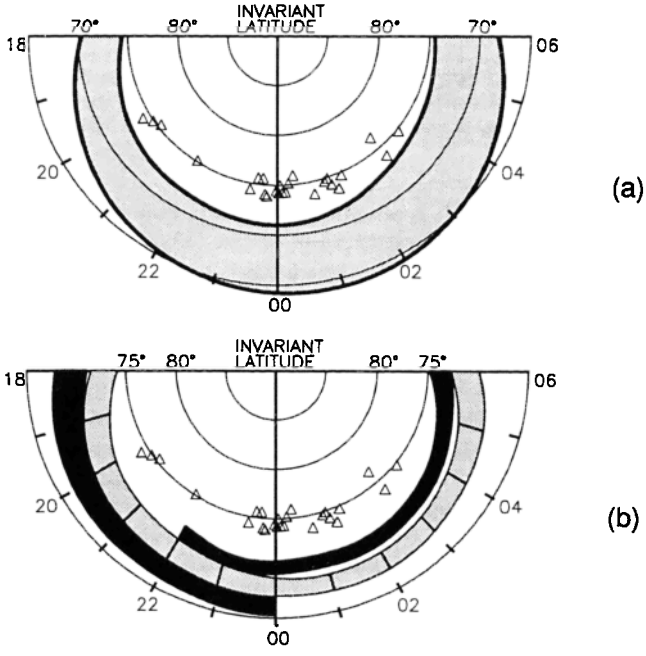

Fig. 2. Cavity occurence plotted on nightside MLT versus invariant latitude polar grids. The (a) grid is overlayed with the *Feldstein and Starkov* [1967] quiet time oval and the (b) grid is overlayed with the region 1 and 2 current system of *Iijima and Potemra* [1976]. Dark and light shading correspond to downward and upward current regions, respectively.

TABLE 1. Auroral Cavity Summary February 1986 to January 1988

Date	K_p	IMF, B_z/B_y	MLT	Polar Cap Density, $\times 10^4$ el/cm^3	% Depletion Relative to Polar Cap	Width, km	Δ Tube Content, $\times 10^{12}$ el/cm^2	ΔT, s	Evacuation Flux, $\times 10^8$ el cm^{-2} s^{-1}
			20:06	9.1	-35	43			
02/10/86	3^+	N/+	20:21	12.6	-44	59	- 1.0	800	-12.5
			20:36	16.2	-62	74	- 0.5	750	- 7.1
			02:35	6.0	*	*	*	*	*
09/19/86	4^+		02:50	8.1	-54	79	- 0.2	912	- 2.5
			02:50	8.1	-53	49	- 0.1	912	- 1.0
			23:33	6.9	*	*	*	*	*
			23:38	7.1	-47	255	- 0.6	300	-18.2
			23:45	7.6	-50	49	- 0.8	400	-21.1
01/24/87			23:58	6.6	-25	56			
	3^-		00:02	7.6	-27	54	- 0.1	300	- 3.7
			00:07	6.9	-23	38	+ 0.3	300	
			00:12	7.2	-52	75	- 0.3	300	-11.1
			00:17	7.6	-40	74	- 0.3	280	-10.3
			00:25	8.7	-49	67	+ 0.2	360	
			01:11	8.7	-54	90			
01/27/87	1	N/+	01:16	6.5	-39	42	+ 0.3	300	
			01:21	6.6	-43	69	- 2.3	270	-84.9
			01:27	6.6	-41	78	- 1.4	240	-57.2
03/06/87	3^+	S/+	21:49	17.8	-69	35			
03/26/87	3^-		00:52	7.9	-34	23			
12/12/87	3^+		03:15	6.3	*	*	*	*	*
			03:26	8.5	-64	79	- 0.7	660	-10.6
12/18/87	3^+		01:37	5.9	-41	43			
			23:20	9.1	-61	134			
01/21/88	3^+		23:31	6.6	-48	194	- 0.6	670	- 8.7
			23:42	6.6	-44	85	- 1.6	670	-24.8
01/30/88	1^-	S/+	00:04	6.5	-30	200			
			00:15	6.5	-48	90	- 0.2	670	- 3.6
Mean	3		00:32	7.8	-45	82	- 0.7	500	-18.5

* Data not available prior to cavity formation.

Summary of auroral cavities from February 1986 to January 1988. Geomagnetic and IMF conditions, as well as mean polar cap densities are listed for each of 29 scans selected according to the criteria in section 2.2. For cavities that evolve in the time between radar scans, the difference in TEC from 100 to 600 km is listed in column 8. An evacuation flux, determined by dividing TEC by the time between radar scans, is listed in column 10. An asterisk indicates a pre-formation radar scan (data not included in average values listed at the bottom of the table).

for multiple scans, it is possible to calculate how the average TEC changes over the scan time of the radar. Each radar scan was overlayed with a magnetic coordinate grid from the PACE geomagnetic model [*Baker and Wing*, 1989] and electron densities were averaged between field lines spanning the cavities over an altitude range from 100 to 600 km. A "pre-formation" TEC was determined from the radar scan prior to the cavity observation. The difference between the current and previous TEC is listed in the eighth column of Table 1 along with the time between radar scans in column 9. Some TEC differences are positive due to E and F region aurora "turning on" between radar scans with no discernable cavity evolution. For those scans with apparent cavity evolution, the TEC decrease, taken together with the time between radar observations, is expressed as an evacuation flux in column 10. These fluxes will be addressed in the context of flux tube evacuation in the discussion section. Table 1 shows that, on average, auroral cavities occur near midnight with depletions of 45 percent below ambient polar cap F region densities over latitudinal widths of $\sim$ 80 km.

3. CASE STUDY: JANUARY 24, 1987

To this point, only statistical properties of auroral ionospheric cavities have been outlined. The evening of January 24, 1987, provides the opportunity to examine cavity formation and evolution with data from a number of ground and satellite instruments. This night was relatively quiet ($K_p = 3^-$) with evidence of a small substorm in a DE 2 UV global image some two hours prior to cavity formation (J. Craven, personal communication, 1989). The radar beam was scanned continuously in the magnetic meridian from 0127 to 0224 UT during the period of cavity formation and subsequent evolution. Monochromatic all-sky imaging during this period established the local position of the aurora beyond the field of view of the radar to the south; a simultaneous global UV image from the Polar BEAR satellite confirmed that the all-sky imager was detecting the poleward edge of the auroral oval. Plate 2 shows the meridional radar scan from 0206:56 to 0211:56 UT together with the coincident 6300-Å ground-based image and Polar BEAR UV

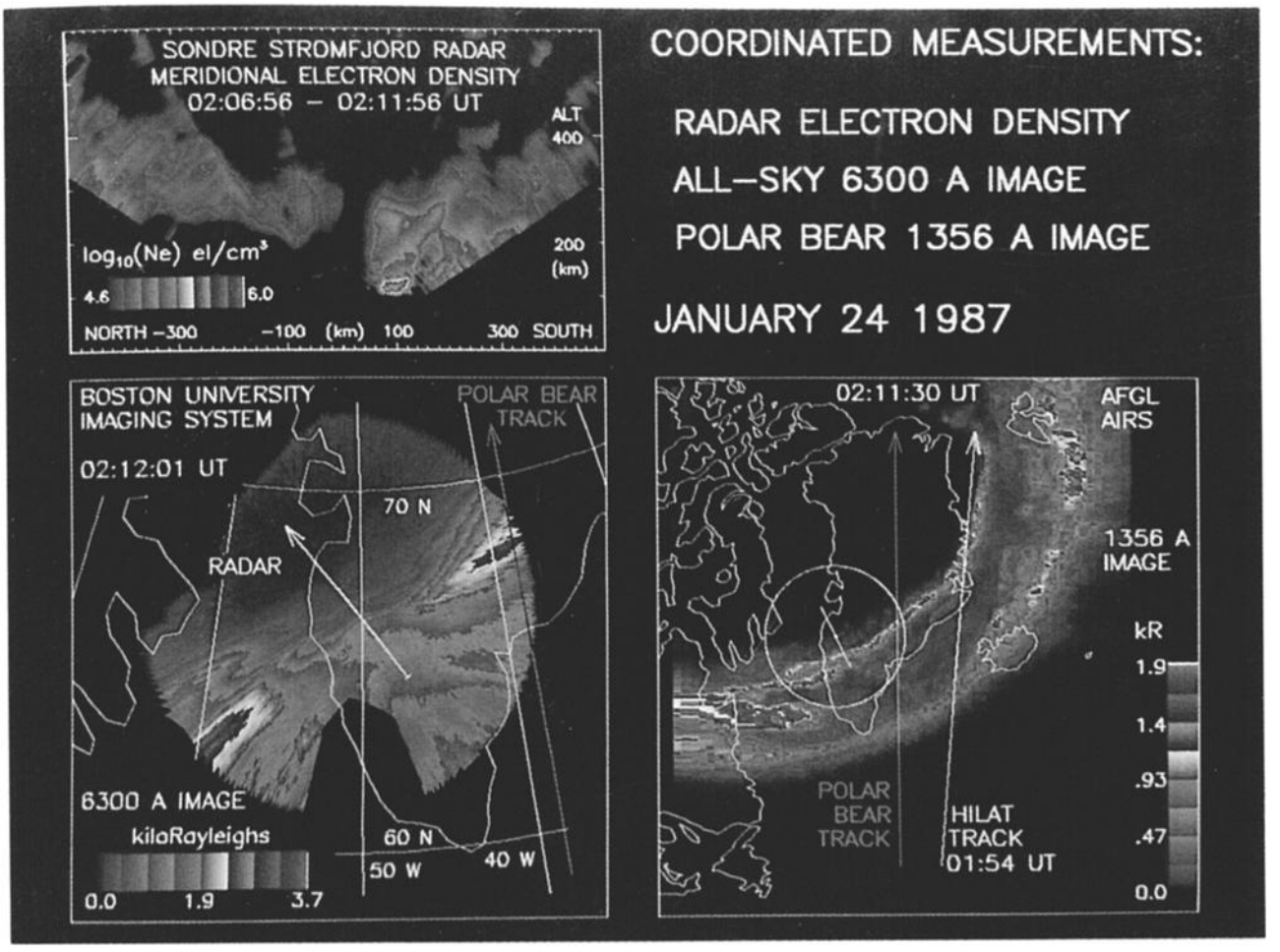

Plate. 2. Montage of coordinated radar, all-sky, and satellite images for the Polar BEAR satellite overflight at 0211 UT on January 24, 1987. The radar panel follows the same spatial and density scale described for Plate 1. The 6300-Å all-sky image recorded at 0212:01 UT has been photometrically corrected, projected onto a reference map (with an assumed 200-km emission height) and color coded from 0.0 to 3.7 kilo-Rayleighs. The radar scan intersection at 200 km and the Polar BEAR groundtrack are indicated by the white and green arrows, respectively. The Polar BEAR 1356-Å image is shown in the third panel and is color-coded from 0.0 to 1.9 kilo-Raleighs. This image has been overlayed with the radar scan intersection and all-sky field of view in white, and the Polar BEAR and HILAT satellite groundtracks in green and yellow, respectively. The UV and all-sky images indicate that the auroral cavity, observed by the radar at Sondre Stromfjord's zenith, is at the poleward edge of the most poleward auroral arc.

image. The 6300-Å image has been masked to cut out obscuration from the radar dish and adjacent mountain. The emission above 75° elevation angle was photometrically corrected and calibrated, and projected onto a geographic grid assuming a mean auroral emission height of 200 km. This assumed height is suggested by measurements from the AE-C spacecraft and the modeling work of *Solomon et al.* [1988]. The Polar BEAR satellite UV 1356-Å image was recorded at 0211 UT by the AFGL AIRS imaging system. This scanning UV imager is described in detail by *Schenkel et al.* [1986]. The Polar BEAR images prior and subsequent to 0211 UT show an auroral oval with a relatively unstructured poleward edge. The 0211 UT UV image shows a midnight oval that is L shell aligned with the same brightness levels at nadir as those just to the west above Sondre Stromfjord. Both the HILAT and Polar BEAR satellites passed overhead of Sondre Stromfjord within 17 min of one another; Figure 3 summarizes the imaging, radar and satellite measurements during this period.

3.1. *Coordinated Radar-Optical Measurements: Meridional $N_e(h)$ Profiles, 6300-Å All-Sky and 1356-Å Satellite Images*

Plate 3 is montage of eight radar scans (including the first three and last four radar scans in the Figure 3 time line) that span the first appearance and subsequent evolution of the cavity. The radar electron density data and associated 6300-Å all-sky images are presented in the same format as in Plate 2. The first 6300-Å image (panel 5) of Plate 3 is overlayed with a geographic grid for reference. Comparison of the radar scans with the 6300-Å images show that the cavity forms at 0132 UT at the poleward edge of the optical emission and follows the edge throughout the next hour. There is no apparent optical signature of the cavity due primarily to the sensitivity of the imaging system. The airglow intensity from dissociative chemistry within the adjacent polar cap F region is calculated to be 150 R, and reduces to 135 R within the cavity. These intensities are below the

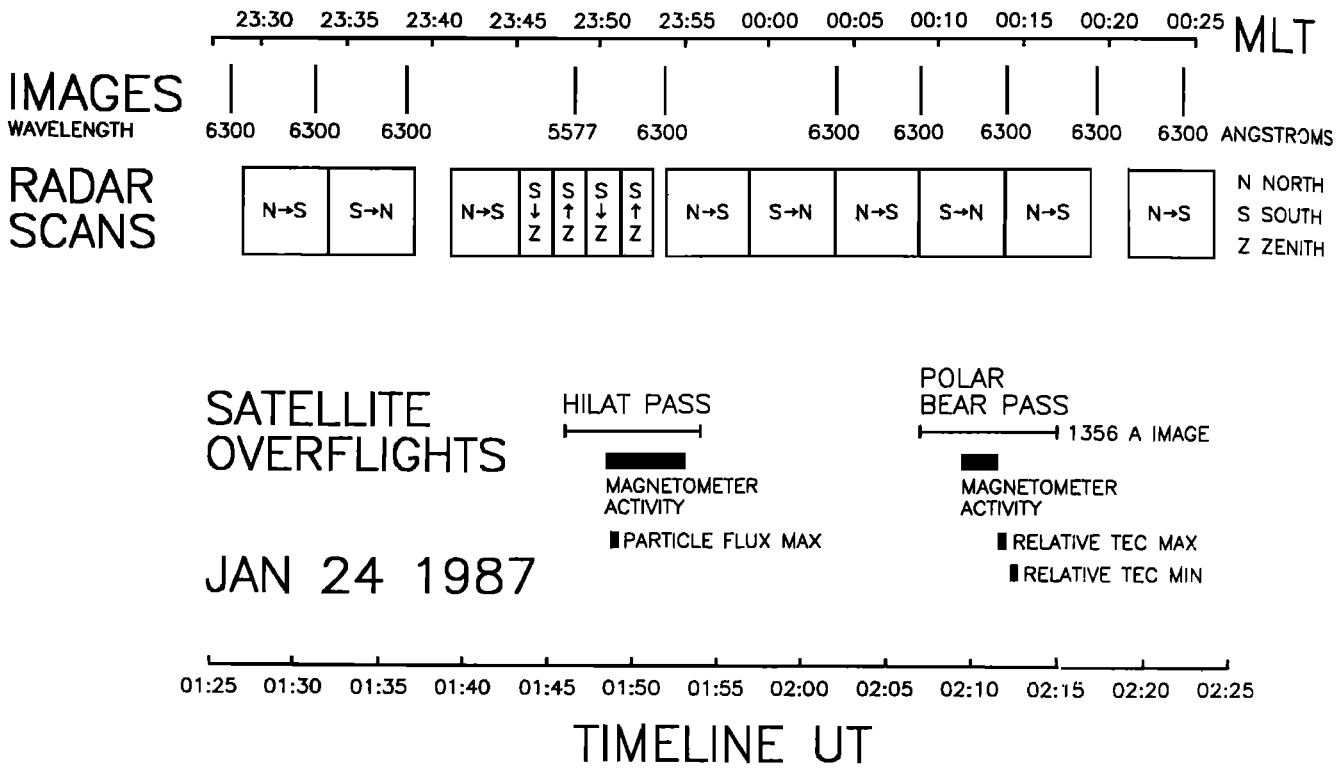

Fig. 3. Time line for the coordinated all-sky imaging, radar, and satellite data recorded during the January 24, 1987, case study.

sensitivity threshold of the imager (configured to saturate for 3.7 kR, bright aurora). The all-sky 6300-Å images did verify the absence of previously mentioned blobs, patches and polar cap arcs, thus satisfying the selection criteria for this period. The UV image in the third panel of Plate 2 shows an edge of bright (~ 1 kR) emission at the edge of the auroral oval in good spatial agreement with the location of bright (~ 2 kR) 6300-Å emission just south of Sondre Stromfjord's zenith. The prior association of these cavities with the statistical position of the oval can now be refined to an association with the instantaneous oval, at least for this 1-hour period around local magnetic midnight.

3.2. *HILAT Satellite Observations: Particle Precipitation and Magnetometer Results*

The HILAT satellite ground track for the pass at 0146 UT, shown in the third panel of Plate 2, was a low-elevation (31° maximum elevation) transit, and crossed at an equivalent invariant latitude 1300 km to the east of the radar. Thus the satellite did not sample the specific MLT region where the cavity was observed by the radar but did sample the magnetic latitude of formation. Under the assumption that the oval conditions were generally uniform along an L shell, the field-aligned currents inferred from the HILAT cross- track (B_y) magnetometer data are superimposed upon the meridional radar scan at 0151:56 UT in the fourth panel of Plate 3. In this panel, red magnetic field lines denote regions of predominantly upward current and green magnetic field lines denote regions of downward current. Although the observations are separated by ~ 23° in longitude, the downward field-aligned current region is generally colocated with the latitude of the auroral cavity.

3.3. *Polar BEAR Satellite Observations: Total Electron Content and Magnetometer Results*

The Polar BEAR satellite passed over Sondre Stromfjord from 0207 to 0215 UT at high elevation some 690 km east of the cavity location (see Plate 2). The five-frequency Polar BEAR phase-coherent beacon provided line of sight TEC by means of differential phase delay and is described in detail by *Cousins et al.* [1984]. Figures 4a-4c show the magnetometer B_{east}, derived field-aligned current and relative TEC data from this pass, respectively. The satellite line of sight was inclined at approximately 60° elevation angle during the intersection of the auroral E region and associated cavity. The TEC (corrected for slant angle) shows a value of 1.1×10^{12} electrons cm^{-2} at the cavity location adjacent to a relative maximum of 4.7×10^{12} electrons cm^{-2} at the location of auroral E region plasma. The TEC for the coincident radar scan (measured as described in section 2.3) is plotted in Figure 4d. There is no Polar BEAR TEC signature at the location of the cavity due, most probably, to the coarse latitudinal sample resolution (~ 0.3°) of these data. The comparison shows that the Polar BEAR TEC peak occurs at approximately the location of the radar TEC peak (at the location of the E region arc) and that both measurements yield similar TEC difference from the arc latitude to adjacent polar cap latitude. Thus, while displaced somewhat eastward, the Polar BEAR satellite probed ionospheric structure similar to that scanned by the radar.

The Polar BEAR magnetometer data pattern is similar to that measured by HILAT: a series of stong current pairs were detected that diminish as the satellite crosses into the polar cap. This similarity lends credence to the concept of L shell aligned sheet currents. In the vicinity of precipitation (as

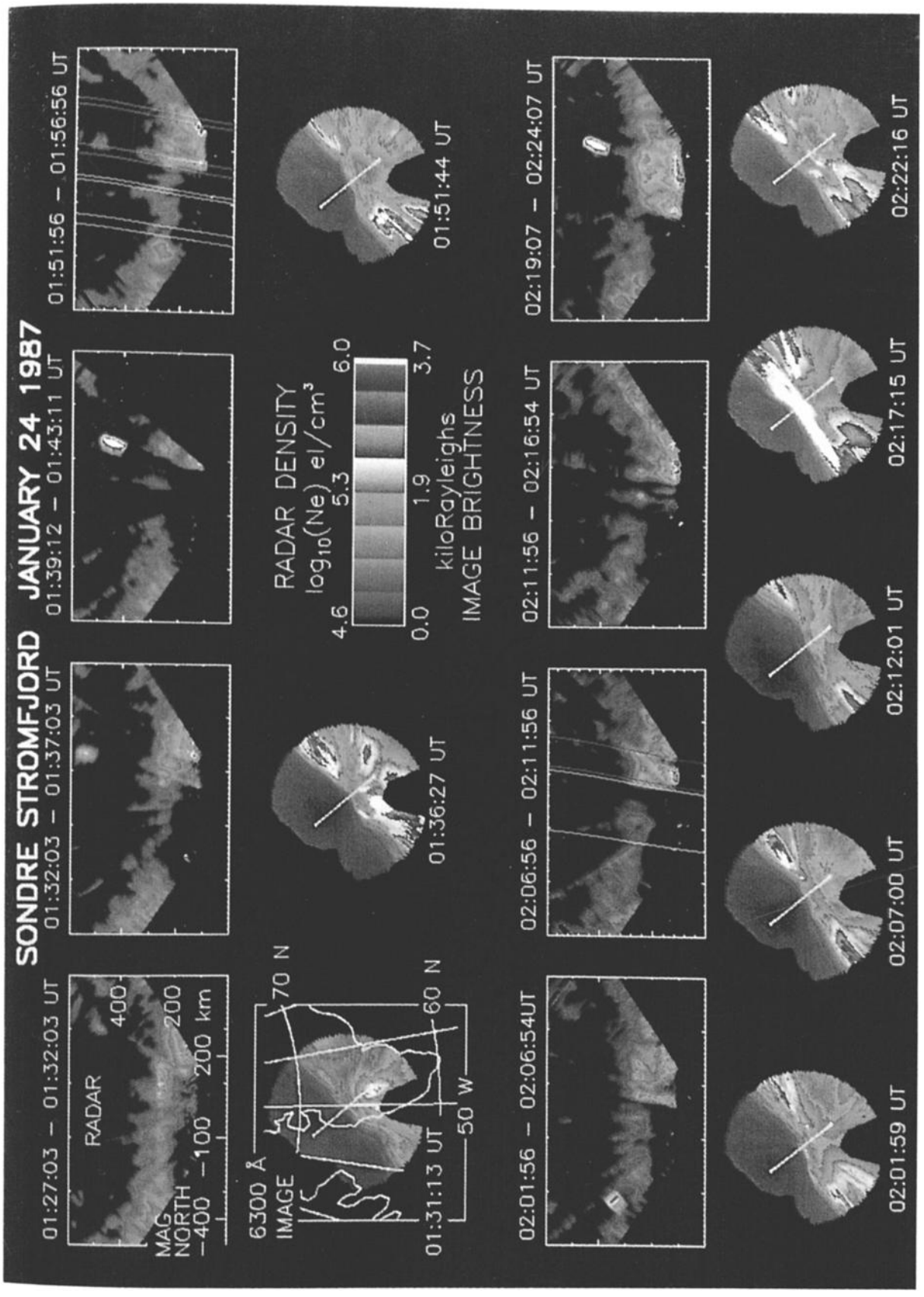

Plate. 3. Radar scans and all-sky 6300-Å images covering the January case study period. Reference grids are included on the first radar and imager panels for clarity. This montage show how the cavity forms at 0132:03 UT and tracks the edge of the instantaneous auroral oval for nearly an hour. The fourth and sixth radar scans were made during overflights of the HILAT and Polar BEAR satellites, respectively. The field-aligned currents inferred from the satellite magnetometers are indicated by color-coded field lines, with red for predominantly upward current, and green for downward current regions. These scans show that the cavity is embedded in regions of downward current (see section 3.3).

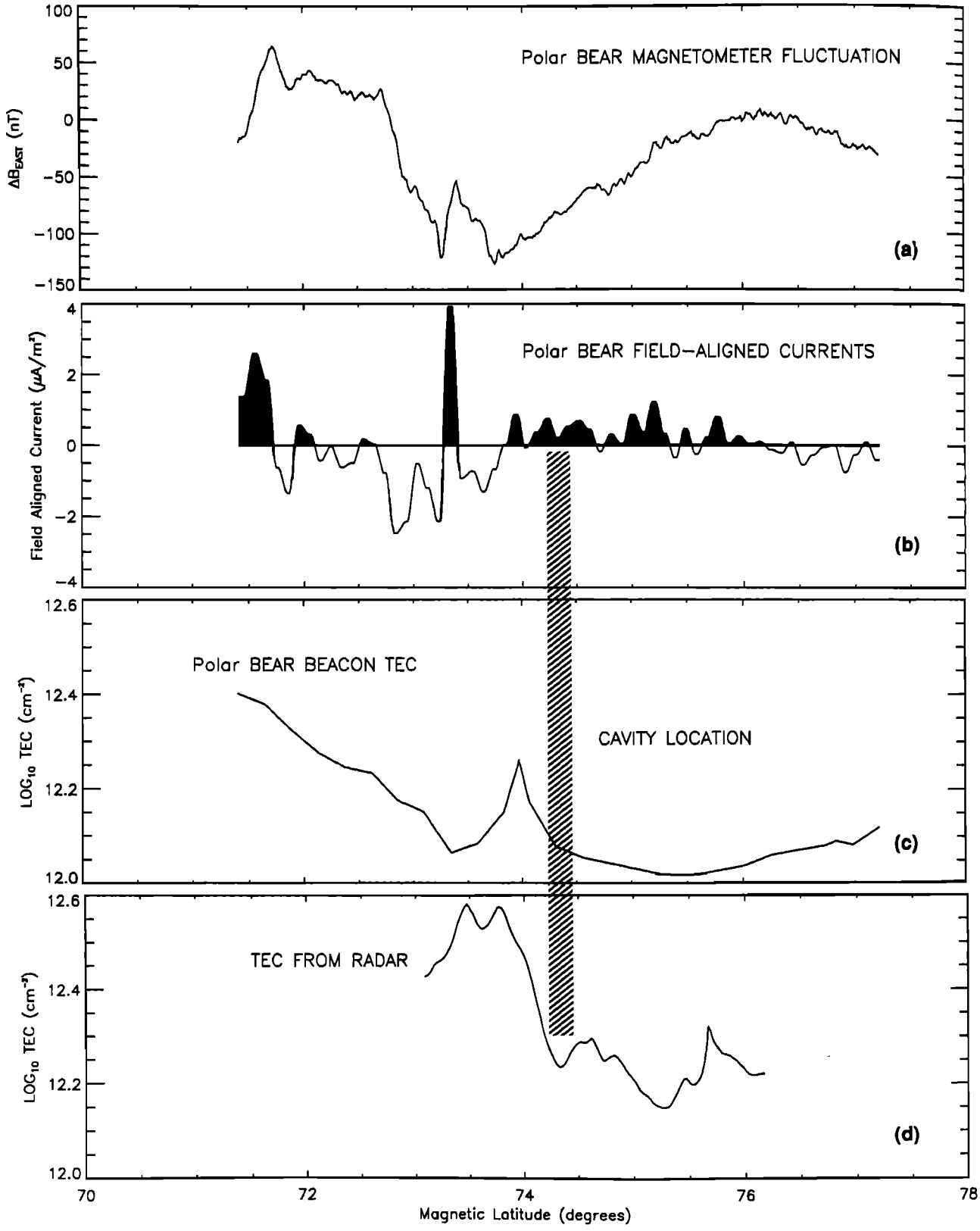

Fig. 4. Polar BEAR magnetometer and TEC measurements compared with simultaneous radar-derived TEC. (a) The residual magnetic east field component after subtraction of the main field. (b) The field-aligned currents inferred from Figure 4a with the conversion of 10 nT s^{-1} to 1 μA m^{-2} and 0.2 Hz low-pass smoothing. Downward field-aligned currents are indicated by dark shading. (c) The log of Polar BEAR TEC data sampled every 15 s. (d) TEC derived from radar data as described in section 2.3. The vertical cross-hatched bar shows the latitudinal position of the cavity as taken from the sixth radar scan in Plate 3. Note that the cavity is located within a region of downward field-aligned current.

defined by enhanced 6300-Å emission which occurs above the latitude of dense E region plasma), the magnetometer data indicate adjacent, oppositely directed field-aligned currents with magnitudes as indicated in Figure 4b. The cavity is located within a downward field-aligned current region of 0.4 μA m^{-2} as mapped to the ionosphere. The field lines corresponding to the location of this current pair have been superimposed on the radar scan taken from 0207 to 0212 UT in the sixth panel of Plate 3. The same red/green color coding has been used to denote up/down current regions. In the same sense as the HILAT magnetometer data, the Polar BEAR upward field-aligned currents are associated with precipitation and downward currents are associated with the region of the cavity. This measurement suggests that the cavity region extends at least 690 km, or 90 minutes of MLT in azmuthal extent.

A firm association of auroral cavities with downward field-aligned currents cannot be determined from such a limited case study; however, the satellite overflights emphasize that cavities are a boundary phenomena probably associated with the transition from upward region 2 to downward region 1 currents near magnetic midnight [*Iijima and Potemra*, 1976]. In a study of six Triad satellite overflights of the Chatanika radar in the morning sector, *Senior et al.* [1982] found that the transition from upward region 2 to downward region 1 currents is collocated with the poleward edge of E region diffuse aurora; there is also a small field-aligned density depletion in their Figure 3.

3.4. *Radar Observations: Plasma Drift, Temperature, and Enhanced Backscatter*

The radar measurements of ion line of sight velocity in the meridional plane can help determine the probable convection pattern during the observation of this auroral cavity. Figure 5a is a line of sight velocity scan which indicates uniform antisunward flow in the F region from zenith to the poleward horizon. South of the radar zenith the F region line of sight velocities are small and disorganized, indicating little southward meridional flow. The shear just over zenith can be inferred from the E region Pedersen drift measured in the 120-km range gate. These drifts are essentially zero north of zenith (corroborating the notion of uniform antisunward flow in the F region) and become southward south of zenith. This implies an eastward zonal flow in the F region south of zenith. Figure 5b shows a subsequent meridional velocity scan when the F region drifts are predominantly antisunward over the entire radar field of view. In addition, a small but uniform eastward component can be inferred from the E region drifts. This local time evolution from a shear at zenith to antisunward flow would be the anticipated meridional pattern change if the edge of a dawnside convection cell were near the radar zenith at midnight.

The *Heppner and Maynard* [1987] empirical convection model can be used to help interpret the meridional flow during this period by comparing samples of the model to the radar line of sight velocities. Figures 5c and 5d represent the best match of the the model for the $K_p = 3$ conditions during this period. The electric fields given by the *Heppner and Maynard* [1987] potentials have been used to calculate a velocity field with the PACE geomagnetic coordinate model and the IGRF85 magnetic field model [*International Association of Geomagnetism and Aeronomy (IAGA)*, 1985]. The resulting velocities have been rendered as line of sight quantities. The polar velocity field is shown in Figure 6, depicting the southwestern edge of a large dawnside convection cell near Sondre Stromfjord.

The cavity and associated arc move poleward during the sixth and eighth radar panels of Plate 3 (0207 UT to 0219 UT). Two line of sight velocity scans during this period are shown Figures 7a and 7b. These scans show general equatorward drift at F region altitudes with E region evidence of enhanced eastward drift north of radar zenith. In order to assess the total $\mathbf{E} \times \mathbf{B}$ drift pattern, a height-dependent model of Hall and Pedersen mobilities has been run for both scan times [*Heelis and Vickrey*, 1990] and the plasma velocity vector rotation with altitude estimated [see *de la Beaujardiere et al.*, 1977]. Figures 7c and 7d show a view, in the horizontal plane, of the total $\mathbf{E} \times \mathbf{B}$ flow pattern given from this analysis for scans in Figures 7a and 7b, respectively. These patterns display larger eastward drifts than implied by Figure 6 and show ~ 300 m s^{-1} drift across the arc. Figure 7c shows a strong shear just north of the E region arc. This sheared flow at 0207 UT is similar to the sheared flow measured at the poleward edge of auroral arc by *Weber et al.* [1991]. Their observation of the poleward motion of a midnight arc relative to ~ 500 m s^{-1} equatorward $\mathbf{E} \times \mathbf{B}$ flow is not unlike the poleward motion of the cavity and associated arc described herein. This relative motion is presented by *Weber et al.* [1991] as evidence for a region undergoing reconnection. Thus it appears that the poleward motion of the cavity is not governed by the bulk $\mathbf{E} \times \mathbf{B}$ flow but is related to electrodynamic variations.

The ion temperature measurements made at 0207 UT and 0212 UT are displayed below corresponding ion velocity plots in Figures 7e and 7f. The T_i hotspot in the 0206:56 UT scan is located south of a region of strong eastward flow (as indicated from the E region drift) and is colocated with the auroral cavity (Plate 3, sixth radar panel). This hotspot, most probably an indication of maximum Joule heating in the vicinity of the arc, suggests that F region plasma may have been depleted through enhanced vertical diffusion or chemical recombination. Both mechanisms, operating alone or together, have been invoked to study F region density structure by *Schunk et al.* [1975], *Basu et al.* [1984] and *Winser et al.* [1986]. If one makes the further assumption that a dawnside cell is moving plasma out of the meridional plane at zenith, then the neutral wind can be caught in a sheared ion flow resulting in an increased slip velocity ($\mathbf{V_i}$ - $\mathbf{U_n}$). This may further enhance chemical loss. Unfortunately, this scan is the only coincident measurement of enhanced T_i with an auroral cavity made during the case study period. Even if cavities were well correlated with enhanced ion temperatures, the discussion, in section 4.2, will show that these two processes alone are not sufficiently rapid to explain the cavity formation time.

For five of the eight radar scans shown in Plate 3, there exist high-altitude regions of intense radar backscatter typically located on a field line that intersects dense E region plasma. These "enhanced radar backscatter," (ERB) regions, which resemble satellite echoes, occur to the south of the radar zenith for the 15 min spanned by the first three panels of Plate 3 and remain on the same field line (at lower altitude) for the second and third panels. Analysis of the ISR spectra for this ERB event indicates a distorted ion acoustic wing morphologically similar to that reported by

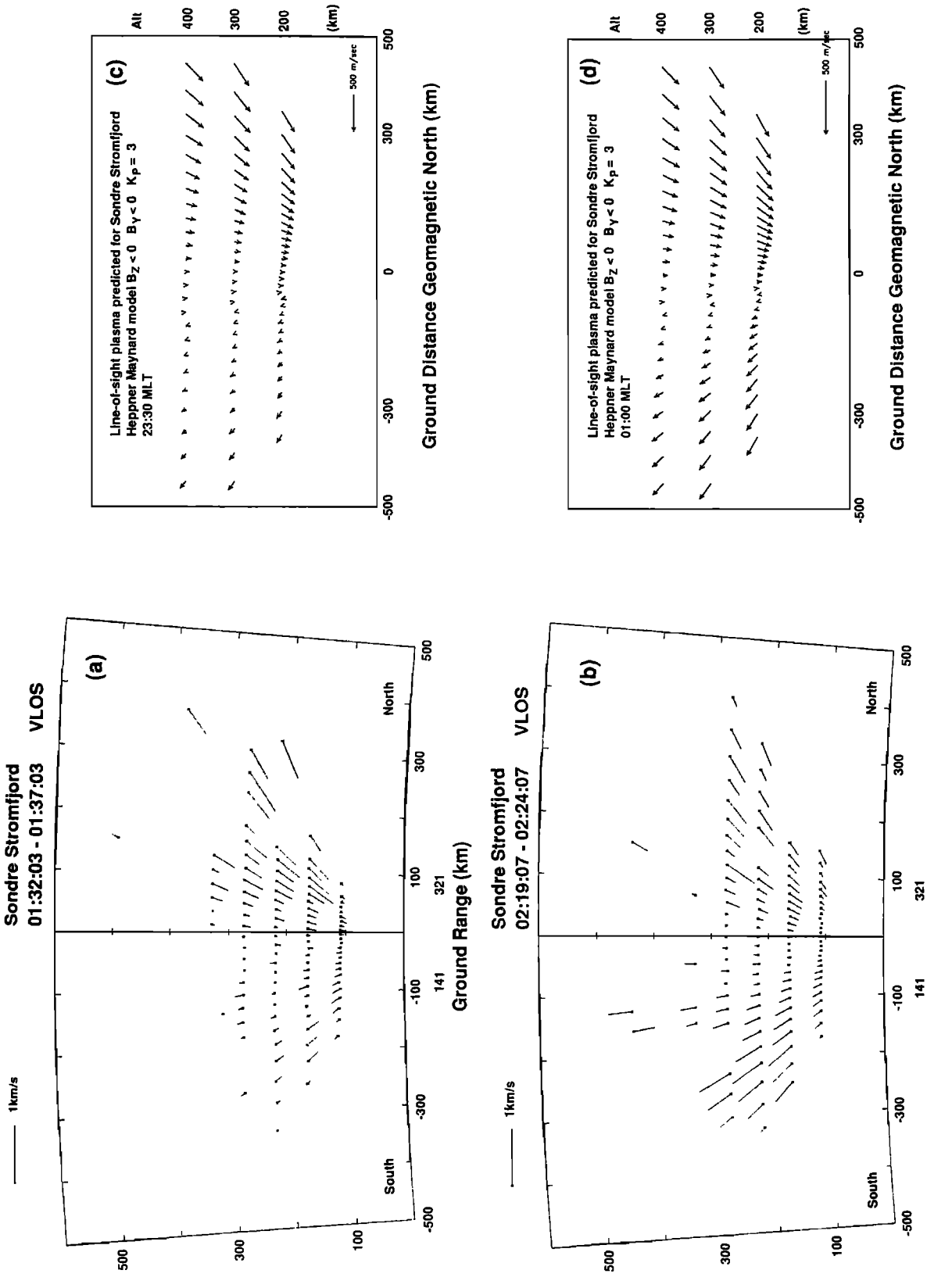

Fig. 5. Comparison of line of sight ion drifts from Sondre Stromfjord on January 24, 1987, with a best fit *Heppner and Maynard* [1987] convection model. Potentials given by this model were converted to three dimensional drifts and rendered as line of sight velocity patterns visible from Sondre Stromfjord. Model patterns, parameterized by IMF and K_p, were then compared with measured drift patterns to determine the best fit for general morphology. (a) Observed ion velocities during a period with the an apparent shear (or rotation) at zenith, and (b) measurements typical for later in the evening when the pattern seems more uniformly antisunward (north to south). (c) and (d) The modeled patterns that best correspond to Figures 5a and 5b, respectively. This model suggests that the IMF B_z and B_y components were negative.

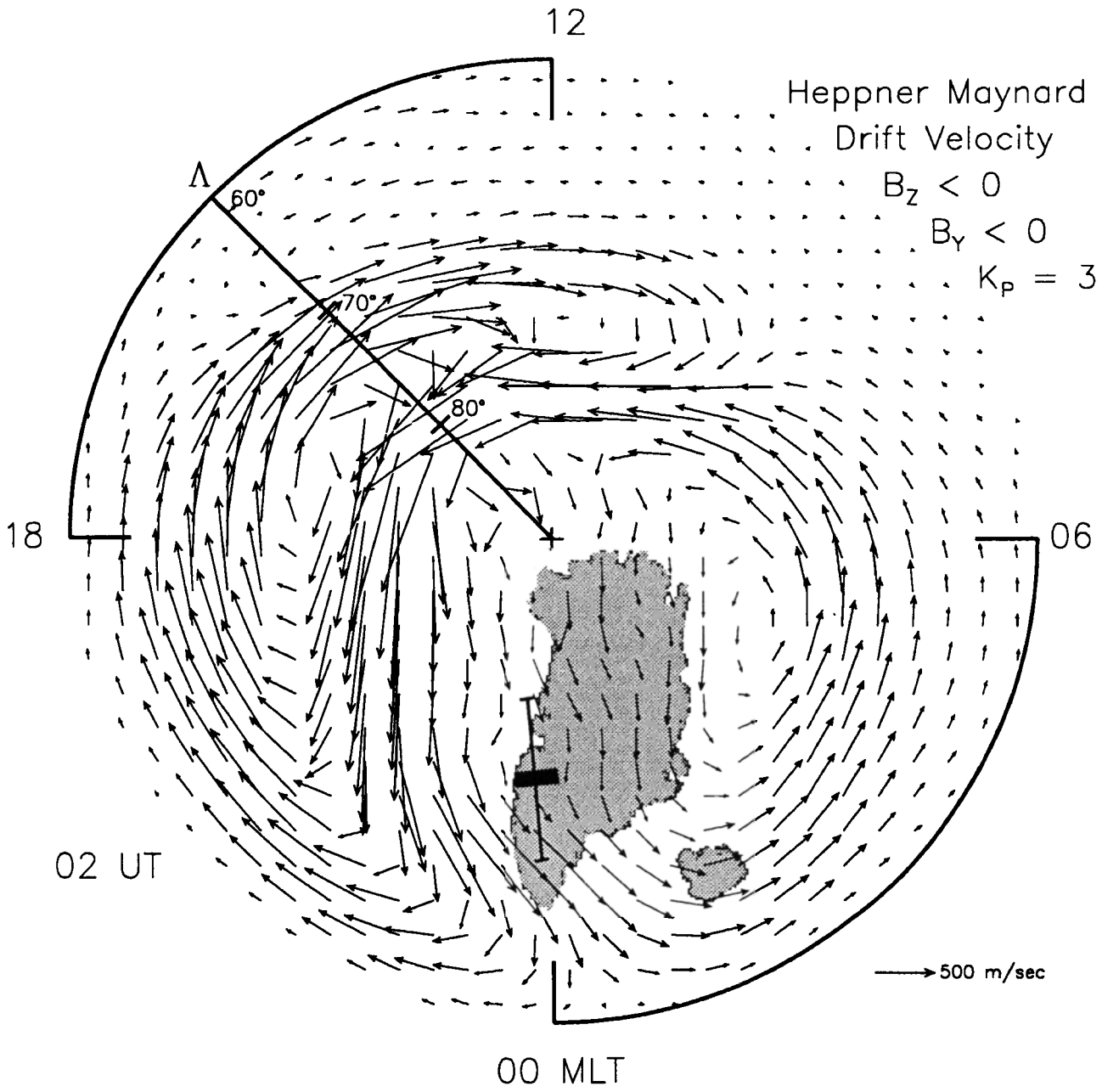

Fig. 6. A polar view of the candidate *Heppner and Maynard* [1987] convection model for January 24, 1987, at 0200 UT. This velocity pattern is the global projection of the magnetic south and east components of the best fit model shown in Figure 5. For this model, the cavity observations are indicated by the thick bar and are located at the southwestern edge of a large dawnside cell.

Foster et al. [1988] and *Rietveld et al.* [1991] in their studies of field-aligned current driven instabilities. Spectral enhancements of this type have been shown by *Collis et al.* [1991] to correspond to intense field-aligned current pairs, and were associated with intense red aurora in the same study. In the current study, the coincident measurement of intense 6300-Å emission (second image panel, Plate 3) at the location of these distorted spectra suggests a consistent picture of auroral cavities observed in the vicinity of intense field-aligned current structure. Not all cavities are observed coincidently with ERBs, however; in fact these five observations represent the only simultaneous measurements in the 29 selected scans.

4. DISCUSSION

Candidate mechanisms for cavity formation can be examined with the aid of the F region continuity equation tailored to the winter nighttime polar cap:

$$\frac{\partial N}{\partial t} = P - \beta N + \nabla\cdot\left(\mathbf{D}\nabla N + N\mathbf{V_p} + \frac{\mathbf{J}}{q}\right) \quad (1)$$

where P is production from polar rain and resonantly scattered solar EUV radiation, βN is chemical loss through charge exchange and subsequent recombination, $\mathbf{D}\nabla N$ includes both transverse and field-aligned diffusive flux, $N\mathbf{V_p}$ represents both plasma $\mathbf{E} \times \mathbf{B}$ and polar wind flux, and $\mathbf{J}$ and q are the current vector and unit charge, respectively,

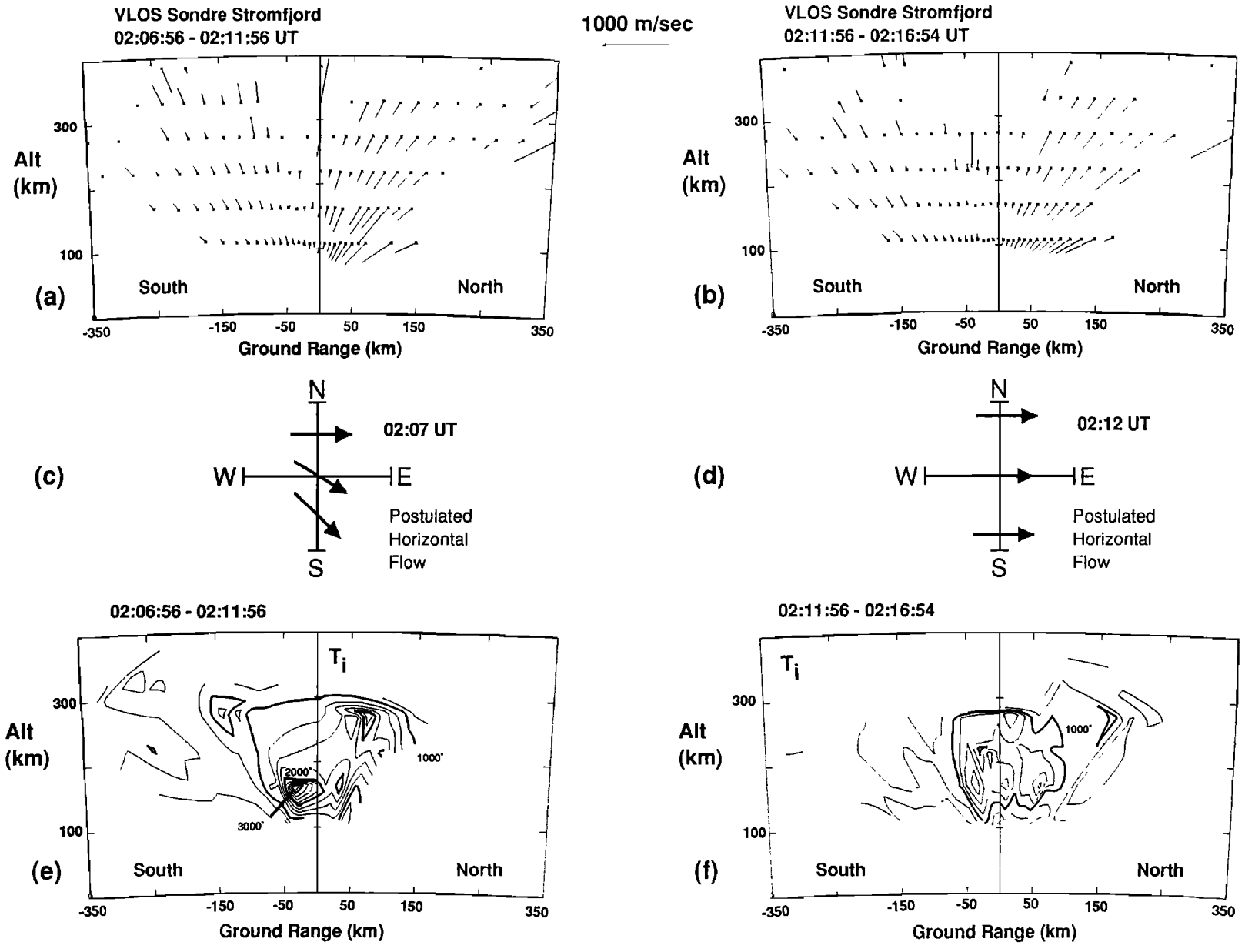

Fig. 7. Comparison of line of sight ion velocities and ion temperatures for two sequential radar scans during which the cavity moved sunward. (a) and (b) The dominant F region flow direction appears antisunward. The Pedersen drift (at 120 km), however, implies significant zonal flow at F region altitudes. (c) and (d) The corresponding total F region horizontal flow when the Pedersen drift component is included. This component has been determined from a height-dependent model of ion mobilities. (e) Elevated temperatures are measured at the position of a significant shear in Figure 4c. (f) This T_i hotspot vanishes within 5 min.

where $\mathbf{J} = nq(\mathbf{V_i} - \mathbf{Ve})$.

4.1. *Production Term*

The production term includes ionization from polar rain and scattered solar EUV radiation but ignores photoionization from direct EUV photons as the solar zenith angle is greater than 120° in the data base considered. For wintertime conditions in the polar cap, estimates of ionization can be made from the 100-eV polar rain fluxes reported by *Winningham and Heikkila* [1974] at approximately 5 ions cm^{-3} s^{-1}. This is of the same magnitude as the 1 ion cm^{-3} s^{-1} production rate calculated by *Knudsen et al.* [1977] for resonantly scattered EUV photons. Thus the composite production rate in the polar cap is less than 10 ions cm^{-3} s^{-1} and will be considered insignificant. For the balance of the discussion, the continuity equation is written as loss and transport dominated:

$$\frac{\partial N}{\partial t} = -\beta N + \nabla \cdot \left(\mathbf{D} \nabla N + N \mathbf{V_p} + \frac{\mathbf{J}}{q} \right) \quad (2).$$

Each of the four remaining terms will be evaluated in the following discussion.

4.2. *Chemical Recombination*

F region plasma loss through charge exchange and subsequent dissociative recombination is a well understood process that is linearly dependent on plasma density for the initial rate limiting reactions. For an oxygen dominated plasma, the familiar reactions,

$$O^+ + N_2 \xrightarrow{k_1} NO^+ + N \quad (3)$$

$$O^+ + O_2 \xrightarrow{k_2} O_2^+ + O \quad (4)$$

have "effective" temperature (T_{eff}) dependent rate coefficients k_1 and k_2. T_{eff} is the thermdynamic quantity that allows the precise formulation of rate coefficients k_1 and k_2 in terms of species temperature and ion-neutral velocity difference. *Schunk et al.* [1975] were the first to relate the laboratory measured ion energy dependence of k_1 and k_2 to an ionospheric environment where T_i and relative ion-neutral (slip) velocity may be greatly enhanced. *St. Maurice and Torr* [1978] generalized the laboratory measurement of O^+ charge exchange rates to the non-Maxwellian thermodynamic conditions sometimes found in the Earth's ionosphere and presented an analytic form for $k_1(T_{eff})$ and $k_2(T_{eff})$ by expressing T_{eff} in terms of the ion temperature, neutral temperature and slip velocity. Assuming F region altitudes and an oxygen dominated plasma, T_{eff} can be approximated by

$$T_{eff} \simeq \frac{T_n}{2} + \frac{T_i}{2} + \frac{\mu U^2}{3k} \quad (5)$$

where U is the slip velocity and μ the ion-neutral reduced mass. Within a reasonable range of high-latitude temperatures and slip velocities, values of $k_1(T_{eff})$ and $k_2(T_{eff})$ can vary over two orders of magnitude, with canonical values of,

$$k_1(T_{eff}) \sim 1 \times 10^{-12} \text{ cm}^3\text{s}^{-1}, \quad (6)$$

$$k_2(T_{eff}) \sim 2 \times 10^{-11} \text{ cm}^3\text{s}^{-1} . \quad (7)$$

The composite loss rate β (s^{-1}) for these two reactions is given by

$$\beta = k_1[N_2] + k_2[O_2] \quad (8)$$

which displays an approximately barometric decrease with altitude. Increasing T_n also has the added effect of increasing the concentration of $[O_2]$ and $[N_2]$ at F region altitudes and further enhances loss by increasing the molecular reservoir available for charge exchange. Thus a sudden, localized heating of the neutral atmosphere might provide a sufficiently large loss rate to create a cavity in the observed formation times. This hypothesis can be tested against the actual loss rate predicted for the ion temperatures measured during the cavity formation sequence of Plate 3. Curve A of Figure 8 compares the decay time ($\tau = \beta^{-1}$) for the measured ion temperature profile measured in the polar cap during the radar scan at 0127:03 UT (panel 1, Plate 3) with the observed cavity formation time (vertical bar). The measured ion temperature profile has been determined by averaging nine records when the radar probed the F region around zenith. For this curve, zero slip velocity and the MSIS-86 neutral temperature of 725 $K°$ have been assumed [*Hedin*, 1987]. Curve B shows how the decay time decreases as T_{eff} is increased by assuming that the slip velocity is 2 km s^{-1} and the neutral temperature is 2000 $K°$. Curve C shows the minimum decay time profile with the additional assumption that the ion temperature profile is enhanced to two standard deviations above the nine record mean. In order to estimate the maximum slip velocity for this period, an empirical horizontal wind model, HWM-87 [*Hedin et al.*, 1988], was run for the magnetic meridian above Sondre Stromfjord and subtracted from the meridional component of the *Heppner and Maynard* [1987] convection model in the same plane. This exercise yields a maximum slip velocity of 280 m s^{-1} for the cavity formation scan, nearly a factor of 10 lower than the estimate used to calculate the loss time profiles of B and C in Figure 8. Unless the ion temperature greatly exceeds the measurement at 0127:03 UT or the slip velocity is much larger than that estimated by the empirical models, it seems impossible to reproduce the observed cavity formation time with chemistry alone. Moreover, it is difficult to explain why this thermospheric cause would be so localized ($\simeq$ 80 km).

4.3. *Diffusion Effects*

Field-aligned ambipolar diffusion can provide sufficiently large plasma escape fluxes for cavity formation provided there are localized T_i enhancements. Cross-field diffusion, on the other hand, acts in a manner similar to production: that is, it would work to "fill in" the cavities near the strong horizontal gradients at the edge of the auroral oval. For both processes, the diffusion coefficent D and gradient scale length L, must be determined in order to calculate the characteristic diffusion time,

$$\tau = \frac{L^2}{D} , \quad (9)$$

and this τ will be compared to the observed cavity formation time for the radar scan at 0127:03 UT (panel 1, Plate 3).

Cross-field diffusion operates on entire flux tubes and thus a vertically integrated diffusion coefficient, $D_\perp$, must be evaluated along the wall of the cavity at the edge of the auroral oval. *Vickrey and Kelley* [1982] show that this cross-field diffusion can be significantly enhanced at F region altitudes due to the presence of a highly conducting E region. For the dense oval plasma observed during the present study

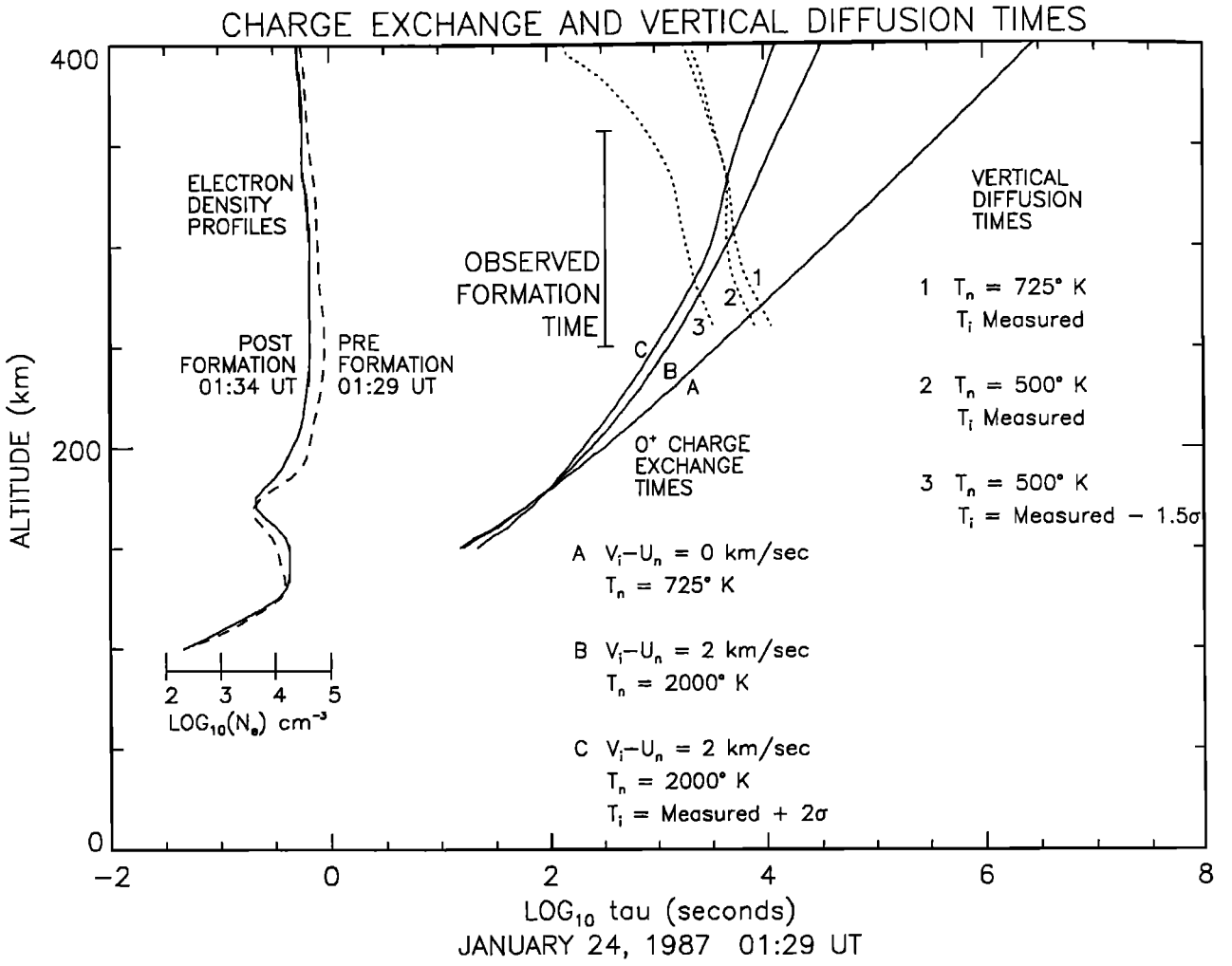

Fig. 8. Calculated charge exchange and vertical diffusion time constants for radar scan at 0129 UT. The electron density profiles before and after cavity formation are shown with a log scale in the left section of the graph. The vertical bar denotes the observed formation time of 300 s. The solid curves A, B, and C indicate the O^+ charge exchange time constant for nominal and perturbed values of ion-neutral slip velocity, neutral temperature and ion temperature. Dotted curves 1,2, and 3 indicate vertical ambipolar diffusion time constant for nominal and perturbed values of neutral and ion temperatures. This figure shows that enhanced chemical loss and diffusion are unable to create auroral cavities in the observed formation time.

period, the perpendicular diffusion coefficient is close to the ion value, $D_{i\perp}$, at the equatorward wall of the cavity. At 0127:03 UT the measured T_i and N_e profiles are known, and with the appropriate MSIS-86 neutral number density and atomic mass profiles the calculated $D_{i\perp}$ is determined to be 85 m^2 s^{-1}. When taken together with the 80 km typical gradient scale length, the perpendicular diffusion time is on the order of several months. Thus, while perpendicular diffusion may play a significant role in determining the shape of cavity edges, it has a negligible effect on structures as large as the cavities themselves.

The altitude-dependent coefficient for field-aligned ambipolar diffusion can be calculated in a similar manner, with the additional knowledge of the measured electron temperature and modeled neutral temperature profiles, T_e and T_n. The ion-neutral, electron-neutral, and electron-ion collision frequencies can be calculated after *Chapman* [1956],

$$\nu_{in}(z) = (2.6 \times 10^{-15}) \times [N_n](z) \times (M_n(z))^{-0.5} \quad (10)$$

$$\nu_{en}(z) = (5.4 \times 10^{-16}) \times [N_n](z) \times (T_n(z))^{0.5} \quad (11)$$

$$\nu_{ei}(z) = (1 \times 10^{-6}) \times (59 + 4.18 \times log_{10}(T_e^3 N_e)) \times T_e^{-3/2} \quad (12)$$

where N_n and N_e are neutral and electron number densities in MKS and M_n is the mass profile in AMU. The resultant altitude-dependent diffusion coefficient determined from *Holt and Haskell* [1965] is

$$d_a(z) = \frac{k_B(T_e(z) + T_i(z))}{m_e\nu_e(z) + m_i\nu_{in}(z)}, \quad (13)$$

where m_e is the electron mass and $\nu_e = \nu_{en} + \nu_{ei}$. Field-aligned diffusion time can now be determined at all altitudes by calculating the ambipolar scale height,

$$H_a(z) = \frac{2\, k_B\, T_i(z)}{m_i\, g}, \quad (14)$$

and evaluating $\tau(z)$ from equation (9) (with H_a representing L). The field-aligned diffusion time profile for the radar scan at 0127:03 UT is plotted as Curve 1 of Figure 8 for the nominal 725° K neutral temperature given by the MSIS-86 model and the nominal T_i profile described previously. Curve 2

shows how this diffusion time can be decreased slightly by reducing the nominal neutral temperature to 500° K, thereby decreasing ν_{in}, and curve 3 is the minimum diffusion time profile with the additional assumption that the measured T_i profile is low by 1.5 standard deviations below the nine record mean. Although lowering T_i decreases d_a, the net effect is to decrease diffusion time since the ambipolar scale height is squared in equation (9). As these three curves show, field-aligned diffusion seems incapable of providing sufficiently rapid topside evacuation to create cavities in the observed formation times.

4.4. *Advecting Gradients, Generalized* $\mathbf{E} \times \mathbf{B}$ *and Current Convective Instabilities*

Previous measurements and modeling studies of F region polar plasma enhancements by *Sojka et al.* [1981], *Kelley et al.* [1982], *Weber et al.* [1984], and *Robinson et al.* [1985] emphasize the central role that the high-latitude convective $\mathbf{E} \times \mathbf{B}$ field has in defining the global position, decay history and horizontal distortion of ionization structure. If the particular flow field depicted in the *Heppnard and Maynard* [1987] pattern of Figure 6 is a reasonable description, then these cavity observations have been made at the edge of a large dawnside convection cell. Modeling by *Robinson et al.* [1985] shows the evolution of an ionization enhancement, initially placed on a duskside streamline of a *Heelis et al.* [1982] convection pattern, from a circular blob to a latitudinally narrow structure. The duskside blob distorts by thinning out along the $\mathbf{E} \times \mathbf{B}$ streamlines and creates a narrow medium scale structure at magnetic midnight. For the current study of wintertime nightside ionization depletions, there seems to be no reason why pre-existing electron density depletions deep in the polar cap would not be subject to the same convective distortion, resulting in latitudinally narrow cavities within the radar's field of view. If the measurements of the horizontal electron density distribution and convection velocity in this study were of sufficient resolution and spatial coverage, one would then expect to see an elongation of these cavities aligned with the $\mathbf{E} \times \mathbf{B}$ flow streamline. While the all-sky imager data support the notion of an L shell aligned cavity, the flow streamlines in Figures 6, 7c, and 7d have a significant meridional component. Thus for one period of the case study this cavity may not be flow-aligned. The meridional radar scans employed throughout the creation of this data base, as mentioned before, unfortunately preclude the definition of extended zonal morphologies (without invoking models). A follow-on experiment will focus on the horizontal convection field in the vicinity of cavities by direct measurement.

Although the edge of the oval is visible throughout this period, it is not stationary, and its motion could be due to local plasma production and/or structuring, not convection. An analysis of the generalized $\mathbf{E} \times \mathbf{B}$ instability for the assumed flow pattern of Figure 6 yields a growth time for perpendicular structure on the scale size of a cavity of 1000 s. For the observed 300-s formation time of auroral cavities, the poleward wall of the oval should, therefore, exhibit little growth of perpendicular structure on the scale of a cavity width.

As pointed out in the radar observations of section 3.4, the apparent motion of the cavity seems to run counter to the measured meridional drift. For the 1-hour case study, the cavity tracks the edge of the oval during significant changes in the meridional component of $\mathbf{E} \times \mathbf{B}$ drift. However, if auroral cavities are due to the action of convection upon existing depletions deep in the polar cap, why should the velocity field always conspire to bring the depletion to the edge of the oval? This scenario, while unlikely, should be tested against a radar data set in which the horizontal velocity field and plasma density are adequately sampled.

4.5. *Field-Aligned Current Evacuation*

The close association of F layer auroral cavities with the boundary of the auroral oval, specifically with the poleward edge of precipitating electrons, and (in a few cases) with regions of enhanced radar backscatter, suggests that thermal plasma is being evacuated to accommodate the magnetospherically imposed current system. Figure 9 is a schematic drawing of the closure of a field-aligned current pair at the edge of the auroral oval. The meridional plane is shown in Figures 9a and 9b during a cavity formation event. Figure 9c shows a view of the horizontal plane prior to cavity formation. In this schematic, the downward current in the polar cap is closed directly to the auroral oval. Current closure parallel to the oval and poleward of the cavity is ignored due to the low Pedersen conductivity ($\Sigma_p^{PC} = 1$ Mho) in the measurements upon which the schematic is based. In order to substantiate this view, one must evaluate the necessary range of currents, compare this to the Polar BEAR magnetometer observations, and use the radar-derived conductivity structure to see if the ionosphere can supply the needed current.

Since the first suggestion of *Block and Fälthammar* [1968] that Birkeland currents could modify the local thermal plasma concentration, there have been theoretical disagreements with this mechanism [e.g., *Schunk and Walker*, 1969] as well as numerous auroral zone measurements of field-aligned currents in the vicinity of discrete arcs. *Cloutier et al.* [1970] flew a vector magnetometer over a stable arc and measured downward field-aligned currents at the arc boundary carried by low-energy electrons. *Klumpar and Heikkila* [1982] used the ISIS 2 soft particle spectrometer to identify 10- to 100-eV field-aligned electron fluxes from the ionosphere at current densities of approximately 1 μA m^{-2}. *Bythrow et al.* [1984] used the same HILAT magnetometer as used in the current study to measure 94 μA m^{-2} downward field-aligned currents at the edge of eveningside discrete UV aurora and verified a nearly simulataneous electron flux sufficiently large to carry the current.

The evacuation fluxes of column ten in Table 1, when expressed as field-aligned currents, span a range from 0.16 to 13.6 μA m^{-2} and are thus consistent with the nominal location and intensity of high-latitude field-aligned currents. This equivalent evacuation current has been averaged over the typical 300-s time between radar scans, and thus the minimum formation time and maximum evacuation current have not been established. A lower bound on cavity formation time can be estimated by requiring that the escaping thermal flux be limited by the ion acoustic velocity. For an ion acoustic velocity, v_{ia}, of 3 km s^{-1}, the maximum evacuation current is $J_\parallel = qN_F V_{ia}$, where N_F is the F region density. For the observations summarized in Table 1, this yields a maximum field-aligned current of approximately 40 μA m^{-2} and a minimum cavity formation time of 30 seconds.

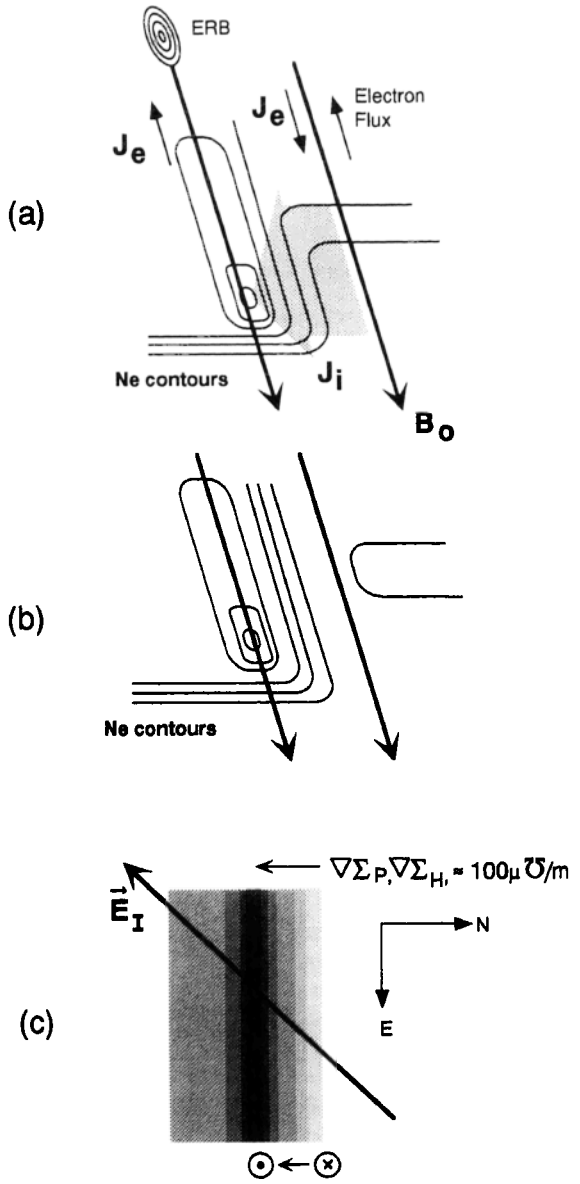

Fig. 9. Schematic drawing of cavity formation from field-aligned currents. (a) A vertical slice through the edge of the auroral oval (in the vicinity of closing up and down field-aligned currents) prior to cavity formation. A possible ERB is shown above a region of dense auroral plasma. Height dependant ion current flowing into the oval from the polar cap is indicated by the shaded arrow. (b) In this scheme, downward current depletes the flux tube of thermal electrons until the cavity forms. (c) A horizontal view of the poleward edge of the oval, with dark shading representing dense plasma. A modeled ionospheric electric field (from Figure 6), as well as calculated conductivity gradients from the radar scan at 0127:03 UT have been assumed. This scenario will support a closure of approximately 1 μA m^{-2} through ion Pedersen currents.

For the specific observations of January 24, 1987, when the cavity formed during the HILAT and Polar BEAR magnetometer overflights (see Plate 3), the estimated field-aligned currents from the evacuation fluxes, 0.6 and 1.8 μA m^{-2}, are significantly larger than the currents estimated from the satellite magnetometers, 0.12 and 0.35 μA m^{-2}, respectively. If the formation current operated for only 30 s, then the satellite may have missed the peak of the event. However, the discrepancy may also be due to the small scale size of the current pairs and the smoothing of the magnetometer data. Moreover, the signature of a large thermal electron current could be reduced by averaging over a portion of the precipitation current. The maximum Polar BEAR downward field-aligned current of 1.2 μA m^{-2}, measured at 0209:12 UT over the oval, is close to the average required evacuation current.

In order to calculate the maximum horizontal current divergence necessary for cavity formation, measured conductivities and conductivity gradients for the radar scan at 0127:03 UT are applied to the situation illustrated in Figure 9c. If the height-integrated Pedersen and Hall conductivities are uniform in the azimuthal direction as shown, and the assumed flow pattern is uniform, then the divergence of horizontal current has contributions only from the latitudinal gradient of Pedersen and Hall conductivities, respectively. These conductivity gradients and eastward component of the electric field are measured directly from the radar and, together with an estimate of the southward electric field give a maximum horizontal current divergence of approximately 1 μA m^{-2}. This is of the same order as the required evacuation current inferred from the radar scan at 0132:03 UT. A polar ionospheric model with self-consistent electric fields, plasma transport and a realistic neutral background is required to provide a quantitative evaluation of the field-aligned evacuation process. While beyond the scope of the present study, such modeling efforts will be the topic for a subsequent paper.

5. CONCLUSIONS

The present study of auroral ionospheric cavities describes narrow field-aligned density depletions in both a statistical and a case study framework. The average location of these cavities is at the poleward edge of the nightside auroral oval. Groundbased 6300-Å and satellite UV images indicate that for the one hour case study of January 24, 1987, the cavity tracks the poleward boundary of the midnight oval.

Cavity formation by enhanced chemistry, vertical diffusion, advection of horizontal plasma gradients and field-aligned currents has been assessed using high time resolution radar scans that allow an estimate of formation times and evacuation fluxes to be made. With only one observation of enhanced T_i in the vicinity of a cavity (during the case study) and without other evidence of a localized high slip velocity between ions and neutrals, enhanced chemical loss is an unlikely cause of the cavities. While vertical diffusion may affect plasma structure, the calculation of the diffusion time made from radar data requires unrealistically low values of neutral and ion temperatures to match the observed depletion time. In order to match observation, drifting plasma structure would have to consistently convect to the poleward edge of the oval. This seems an unlikely circumstance.

In the case study examined, the cavity marks the boundary between a region with highly structured field-aligned current pairs and a region with less structured, predominantly upward field-aligned currents. From an overflight of the Polar BEAR satellite the cavity is observed to be embedded in a region of downward current (upward moving electrons). The observation of regions with enhanced radar backscatter and associated distorted spectra above the auroral E region and in the vicinity of the cavity make field-aligned current evacuation an attractive explanation for

this phenomena. However, this judgement must be tested against an electrodynamically self-consistent high-latitude model of auroral precipitation, transport, chemistry, and diffusion.

Acknowledgments. This study made extensive use of the coordinated Sondre Stromfjord Incoherent Scatter Radar - HILAT and Polar BEAR satellite database organized at SRI International through the diligent work of Mary McCready. The authors thank the SRI Sondre Stromfjord Incoherent Scatter Radar Facility site crew and the Danish Commission for Scientific Research in Greenland for gathering the raw data in the field. The authors thank Jeffrey Baumgardner at Boston University for his fabrication and fielding of the all-sky monochromatic imager and subsequent assistance with digital image processing. Jose Enriquez was instrumental in developing the image acquisition and analysis software. W. Jeffrey Hughes, Robert Kerr, Henry Rishbeth, Alan Rodger, and George Siscoe provided many helpful comments and suggestions. Work at SRI was supported by NSF Cooperative Agreement ATM88-22560 and by Phillips Laboratory contract F19628-90-K-0036. Work at Boston University was supported by NSF grants ATM-9012786 and ATM-9102557.

The Editor thanks M. T. Rietveld and E. J. Weber for their assistance in evaluating this paper.

REFERENCES

Baker, K. B., and S. Wing, A new magnetic coordinate system for conjugate studies at high latitudes, *J. Geophys. Res., 94,* 9139, 1989.

Basu, S., S. Basu, E. MacKenzie, W. R. Coley, W. B. Hanson and C. S. Lin, *F* region electron density irregularity spectra near auroral acceleration and shear regions, *J. Geophys. Res., 89,* 5554, 1984.

Benson, R. F., and W. Calvert, ISIS 1 observations at the source of auroral kilometric radiation, *Geophys. Res. Lett., 6,* 479, 1979.

Block, L. P., and C.-G. Fälthammar, Effects of field aligned currents on the structure of the ionosphere, *J. Geophys. Res., 73,* 4807, 1968.

Brinton, H. C., J. M. Grebowsky, and L. H. Brace, The high latitude winter *F* region at 300 km: Thermal plasma observations from AE-C, *J. Geophys. Res., 83,* 4767, 1978.

Buchau, J., B. W. Reinisch, E. J. Weber, and J. G. Moore, Structure and dynamics of the winter polar cap *F* region, *Radio Sci., 18,* 995, 1983.

Bythrow, P. F., T. A. Potemra, W. B. Hanson, L. J. Zanetti, C.-I. Meng, R. E. Huffman, F. J. Rich, and D. A. Hardy, Earthward directed high-density Birkland currents observed by HILAT, *J. Geophys. Res., 89,* 9114, 1984.

Carlson, H. C., V. B. Wickwar, E. J. Weber, J. Buchau, J. G. Moore, and W. Whiting, Plasma characteristics of polar cap *F*-layer arcs, *Geophys. Res. Lett., 11,* 895, 1984.

Chapman, S., The electrical conductivity of the ionosphere: A review, *Nuovo Cimento, 4* (10), suppl. 4, 1385, 1956.

Cloutier, P. A., H. R. Anderson, R. J. Park, R. R. Vondrak, R. J. Spiger, and B. R. Sandel, Detection of geomagnetically aligned currents associated with an auroral arc, *J. Geophys. Res., 75,* 2595, 1970.

Collis, P. N., I. Haggstrom, and K. Kaila, EISCAT radar observations of enhanced incoherent scatter spectra: Their relation to red aurora and field-aligned currents, *Geophys. Res. Lett., 18,* 1031-1034, 1991.

Cousins, M. D., R. C. Livingston, C. L. Rino, and J. F. Vickrey, The HILAT satellite multifrequency radio beacon, *Johns Hopkins APL Tech. Dig., 5* (2), pp. 109-113, 1984.

de la Beaujardiere, O., R. Vondrak, and M. Baron, Radar observations of electric fields and currents associated with auroral arcs, *J. Geophys. Res., 82,* 5051, 1977.

Farrell, W. M., M. D. Desch, M. L. Kaiser, and W. Calvert, Evidence of auroral plasma cavities at Uranus and Neptune from radio burst observations, *J. Geophys. Res., 96,* 19049, 1991.

Feldstein, Y. I., and G. V. Starkov, Dynamics of auroral belt and polar geomagnetic disturbances, *Planet. Space Sci., 15,* 209-229, 1967.

Foster J. C., C. del Pozo, K. Groves, and J.-P. St. Maurice, Radar observations of the onset of current driven instabilities in the topside ionosphere, *Geophys. Res. Lett., 15,* 160-163, 1988.

Hedin, A. E., MSIS-86 Thermospheric Model, *J. Geophys. Res., 92,* 4649, 1987.

Hedin, A. E., N. W. Spencer, and T. L. Killeen, Empirical global model of upper thermosphere winds based on Atmosphere and Dynamics Explorer satellite data, *J. Geophys. Res., 93,* 9959, 1988.

Heelis, R. A. and J. F. Vickrey, Magnetic field-aligned effects on ionospheric plasma structure, *J. Geophys. Res., 95,* 7995, 1990.

Heelis, R. A., J. K. Lowell, and R. W. Spiro, High latitude ionospheric convection model, *J. Geophys. Res., 87,* 6339, 1982.

Heppner, J. P., and N. C. Maynard, Empirical high-latitude electric field models, *J. Geophys. Res., 92,* 4467, 1987.

Holt, E. H., and R. E. Haskell, *Plasma Dynamics,* 188 pp., Macmillan, New York, 1965.

International Association of Geomagnetism and Aeronomy Division I Working Group 1, International Geomagnetic Reference Field: Revision 1985, *J. Geomagn. Geoelectr., 37,* 1157, 1985.

Iijima, T., and T. A. Potemra, Field-aligned currents in the dayside cusp observed by Triad, *J. Geophys. Res., 81,* 5971, 1976.

Kelley, M. C., J. F. Vickrey, C. W. Carlson, and R. Torbert, On the origin and spatial extent of high-latitude *F* region irregularities, *J. Geophys. Res., 87,* 4469, 1982.

Klumpar, D. M., and W. J. Heikkila, Electrons in the ionospheric source cone: Evidence for runaway electrons as carriers of downward Birkland currents, *Geophys. Res. Lett., 9,* 873, 1982.

Knudsen, W. C., P. M. Banks, J. D. Winningham, and D. M. Klumpar, Numerical model of the convecting F_2 ionosphere at high latitudes, *J. Geophys. Res., 82,* 4784, 1977.

Persoon, A. M., D. A. Gurnett, W. K. Peterson, J. H. Waite, Jr., J. L. Burch, and J. L. Green, Electron density depletions in the nightside auroral zone, *J. Geophys. Res., 93,* 1871, 1988.

Rietveld, M. T., P. N. Collis, and J.-P. St.-Maurice, Naturally enhanced ion-acoustic waves in the auroral ionosphere observed with the EISCAT 933 MHz radar, *J. Geophys. Res., 96,* 19291, 1991.

Robinson, R. M., R. T. Tsunoda, J. F. Vickrey, and L. Guerin, Sources of *F* region ionization enhancements in the nighttime auroral zone, *J. Geophys. Res., 90,* 7533, 1985.

Robinson, R. M., and S. B. Mende, Ionization and electric field properties of auroral arcs during magnetic quiescence, *J. Geophys. Res., 95,* 21,111, 1990.

Rodger A. S., R. J. Moffett and S. Quegan, The role of ion drift in the formation of ionisation troughs in the mid and high-latitude ionosphere - A review, *J. Atmos. Terr. Phys., 54,* 1, 1992.

Schenkel, F. W., B. S. Ogorzalek, R. R. Gardner, R. A. Hutchins, R. E. Huffman, and J. C. Larrabee, Simultaneous multispectral narrow band auroral imagery (1150 Å to 6300 Å), *Proc. Soc. Photo. Instrum. Eng., 687,* 90, 1986.

Schunk, R. W., and J. C. G. Walker, Discussion of paper by L. P. Block and C.-G.Fälthammar, Effects of field aligned currents on the structure of the ionosphere, *J. Geophys. Res., 74,* 3747, 1969.

Schunk, R. W., W. J. Raitt, and P. M. Banks, Effect of electric fields on the daytime high-latitude *E* and *F* regions, *J. Geophys. Res., 80,* 3121, 1975.

Senior, C., R. M. Robinson, and T. A. Potemra, Relationship between field-aligned currents, diffuse auroral precipitation and the westward electrojet in the early morning sector, *J. Geophys. Res., 87,* 10,469, 1982.

Sojka, J. J., W. J. Raitt, and R. W. Schunk, A theoretical study of the high-latitude winter *F* region at solar minimum for low magnetic activity, *J. Geophys. Res., 86,* 609, 1981.

Solomon, S. C., P. B. Hays, and V. J. Abreu, The auroral 6300 Å emission: Observations and Modeling, *J. Geophys. Res., 93,* 9867, 1988.

St.-Maurice, J.-P. and D. G. Torr, Nonthermal rate coefficients

in the ionospheric: The reactions of O^+ with N_2, O_2 and NO, *J. Geophys. Res., 83,* 969, 1978.

Tsunoda, R. T., High-latitude *F* region irregularities: A review and synthesis, *Rev. Geophys., 26,* 719, 1988.

Vickrey, J. F., and M. C. Kelley, The effects of a conducting *E* layer on classical *F* region cross-field plasma diffusion, *J. Geophys. Res., 87,* 4461, 1982.

Vickrey, J. F., C. L. Rino, and T. A. Potemra, Chatanika/TRIAD observations of unstable ionization enhancements in the auroral *F* region, *Geophys. Res. Lett., 7,* 789, 1980.

Weber, E. J., J. Buchau, J. G. Moore, J. R. Sharber, R. C. Livingston, J. D. Winningham, and B. W. Reinisch, *F* layer ionization patches in the polar cap, *J. Geophys. Res., 89,* 1683, 1984.

Weber, E. J., J. F. Vickrey, H. Gallagher, L. Weiss, C. J. Heinselman, R. A. Heelis, and M. C. Kelley, Coordinated radar and optical measurements of stable auroral arcs at the polar cap boundary, *J. Geophys. Res., 96,* 17,847, 1991.

Winningham, J. D., and W. J. Heikkila, Polar cap auroral electron fluxes observed with ISIS 1, *J. Geophys. Res., 79,* 949, 1974.

Winser, K. J., G. O. L. Jones, and P. J. S. Williams, A quantitative study of the high latitude ionospheric trough using EISCAT's common programmes, *J. Atmos. Terr. Phys., 48,* 893, 1986.

R. A. Doe and M. Mendillo, Center for Space Physics, Boston University, Boston, MA 02215

R. W. Eastes, Geophysics Directorate, Phillips Laboratory, Hanscom AFB, MA 01731

J. F. Vickrey, Geoscience and Engineering Center, SRI International, Menlo Park, CA 94025

L. J. Zanetti, Johns Hopkins University, Applied Physics Laboratory, Laurel, MD 20723

(Received February 10, 1992;
revised June 1, 1992;
accepted July 27, 1992.)